Electronic structure and magnetic properties of the strong-rung spin-1 ladder compound $Rb_3Ni_2(NO_3)_7$

Z. V. Pchelkina,[1,2,*] V. V. Mazurenko,[2] O. S. Volkova,[2,3,4] E. B. Deeva,[3] I. V. Morozov,[3] V. V. Shutov,[3] S. I. Troyanov,[3] J. Werner,[5] C. Koo,[5] R. Klingeler,[5,6] and A. N. Vasiliev[3,4,7]

[1]*M.N. Miheev Institute of Metal Physics UB RAS, Ekaterinburg 620137, Russia*
[2]*Ural Federal University, Ekaterinburg 620002, Russia*
[3]*Lomonosov Moscow State University, Moscow 119991, Russia*
[4]*National University of Science and Technology "MISiS", Moscow 119049, Russia*
[5]*Kirchhoff Institute of Physics, Heidelberg University, Heidelberg D-69120, Germany*
[6]*Centre for Advanced Materials, Heidelberg University, Heidelberg D-69120, Germany*
[7]*National Research South Ural State University, Chelyabinsk 454080, Russia*

(Received 6 February 2017; revised manuscript received 2 April 2018; published 24 April 2018)

$Rb_3Ni_2(NO_3)_7$ was obtained by crystallization from anhydrous nitric acid solution of rubidium nitrate and nickel nitrate hexahydrate. The crystal structure determined on single crystals implies isolated spin-1 two-leg ladders of Ni^{2+} ions connected by $(NO_3)^-$ groups as basic elements. Magnetic susceptibility, specific heat in magnetic fields up to 9 T, magnetization, and high-frequency electron spin resonance studies performed on powder samples show the absence of long-range magnetic order at $T \geqslant 2$ K. Electronic structure calculations and the detailed analysis of the experimental data enable quantitative estimates of the relevant parameters of the $S = 1$ ladders in $Rb_3Ni_2(NO_3)_7$. The rung coupling $J_1 = 10.16$ K, the leg coupling $J_2 = 1.5$ K, and the Ising-type anisotropy $|A| = 8.6$ K are obtained. The scenario of a valence-bond solidlike quantum ground state realized in the two-leg Ni^{2+} ladders is further corroborated by model simulations of the magnetic susceptibility.

DOI: 10.1103/PhysRevB.97.144420

I. INTRODUCTION

The experimental and theoretical search for materials that are physical realizations of quantum spin models on low-dimensional lattices is a main focus of current condensed matter physics. Depending on the lattice geometry, such model materials with spin-$\frac{1}{2}$ demonstrate numerous nontrivial magnetic phenomena, such as Bose-Einstein condensation of the magnons [1], plateaus of the magnetization [2], the resonating valence-bond ground state (triangular lattice), skyrmions [3], and others. In the recent years, prototypical low-dimensional magnetic systems with spin larger than $\frac{1}{2}$ have attracted attention as experimental and theoretical studies on systems with $S \geqslant 1$ open a way to probe the quantum states of model systems which differ from the extreme case of the spin-$\frac{1}{2}$ analogs.

It was an unexpected theoretical discovery that coupling of two spin-$\frac{1}{2}$ Heisenberg quasiordered chains (with infinite correlation lengths) into spin-$\frac{1}{2}$ ladder leads to finite-range correlations and an excitation gap (for a review, see Ref. [4]). The spin-1 single chain displays quite different properties as compared to the spin-$\frac{1}{2}$ chain, too. Its coupled ladder version, i.e., the spin-1 N-leg ladder has been the object of active theoretical research in the last years [5–9]. Like in the chains, the integer and noninteger spin ladders exhibit strongly different properties: using the density matrix renormalization group (DMRG) method, it was shown that for semi-integer spin ladders the spin excitations are gapless for odd legs and gapped for even leg numbers. For integer spin ladders, the spin gap is nonzero for both odd and even number of legs [6]. In particular, the even-leg spin-1 ladder has been found to host a symmetry-protected topological ground state [7]. The presence of anisotropy has been suggested to yield a nontrivial entanglement spectrum even in the unperturbed ground state [8].

In this paper, we report on the structural, electronic, and magnetic properties of the first synthesized rubidium-nickel nitrate $Rb_3Ni_2(NO_3)_7$. By means of thermodynamic and resonance measurements and first-principles numerical simulations, we show that this compound is the physical realization of the strong-rung spin-1 ladder model. The magnetic susceptibility reveals a maximum at about 11 K, which corresponds to singlet-triplet excitations. High-frequency electron spin resonance data clearly prove significant zero-field splitting which is associated with presumingly uniaxial magnetic anisotropy of $|A| = 8.6$ K. The exchange interactions along the legs, the rungs, and between the ladders are numerically obtained along with their microscopic explanation. The experimental data obtained on a multitude of randomly oriented single crystals are compared with simulations by means of the Heisenberg model for independent dimers and ladder by means of exact diagonalization and quantum Monte Carlo methods, respectively. The results support the strong-rung spin-1 ladder scenario with $J_1 = 10.5$ K and $J_2 = 1.6$ K.

In general, spin-gap materials have a singlet ($S = 0$) ground state and the triplet excited states separated from the first one by the energy gap. At a critical value of external magnetic field H_c, the lowest triplet state ($S_z = 1$) intersects the $S = 0$ ground state. This leads to the field-induced magnetic long-range ordering. Among $S = 1$ compounds extensively investigated in this context, one can find the realization of

*pchelkzl@mail.ru

the $S = 1$ coupled spin dimer system with small uniaxial single-ion anisotropy $Ba_3Mn_2O_8$ [10], as well as $S = 1$ quasi-one-dimensional (quasi-1D) compound with large single-ion easy-plane anisotropy $NiCl_2$-4SC$(NH_2)_2$ (DTN) [11,12]. $Rb_3Ni_2(NO_3)_7$ represents an intermediate case of $S = 1$ strong-rung ladder system with comparable value of single-ion anisotropy (the leg coupling is small). We hope that the current research will stimulate the low-temperature investigation of $Rb_3Ni_2(NO_3)_7$ in external magnetic field, in which at low enough temperatures interesting quantum phenomena could be detected.

II. METHODS

The crystalline samples of $Rb_3Ni_2(NO_3)_7$ were synthesized from solution of rubidium nitrate $RbNO_3$ and nickel nitrate hexahydrate $Ni(NO_3)_2 \cdot 6H_2O$ in anhydrous nitric acid. The solution was placed into an evacuated desiccator above the phosphorus anhydrate P_2O_5 and crystallization continued for few weeks until complete removal of the liquid phase. The molar ratio of $RbNO_3$:$Ni(NO_3)_2 \cdot 6H_2O = 2:1$ was used since for the stoichiometric composition of the initial mixture (3 : 2), magnetic admixture of $Ni(NO_3)_2$ was formed together with the main product. The details of the synthesis method of ammonium nitratometallates similar to that used to prepare the title compound are given in Ref. [13].

The green crystals of $Rb_3Ni_2(NO_3)_7$ of about 0.1 mm in lateral dimensions were mechanically separated from the colorless crystals of the rubidium nitrate present in the precipitate. It should be noted that $Rb_3Ni_2(NO_3)_7$ is highly hygroscopic and in air it gradually decomposes into $RbNO_3$ and nickel nitrate hydrates $Ni(NO_3)_2 \cdot nH_2O$ ($n = 2,4,6$). Therefore, the obtained product was stored under argon in sealed ampules and manipulations for the samples' preparation for various studies were performed in a glove box under dry nitrogen or argon atmosphere. During the measurements, special efforts were taken to minimize or avoid the exposure time of the sample to air. However, even shortest exposure to air may lead to deterioration of the sample.

The temperature dependency of the magnetic susceptibility of $Rb_3Ni_2(NO_3)_7$ was measured at $B = 0.1$ T by means of a Magnetic Properties Measurement System (MPMS XL-5, from Quantum Design) while the field dependence of magnetization at $T = 2.4$ K in magnetic fields up to 15 T was studied by means of a home-built vibrating sample magnetometer (VSM) [14]. The specific heat was measured at various magnetic fields up to 9 T by means of a Physical Properties Measurement Systems (PPMS, from Quantum Design).

High-frequency/high-field electron spin resonance (HF-ESR) measurements were carried out using a phase-sensitive millimeter wave-vector network analyzer from AB Millimetré in the frequency range from 40 to 450 GHz and in magnetic fields up to 16 T [15]. For the experiments, a fixed powder sample in an airtight glass vessel was placed in the sample space of the cylindrical waveguide.

The electronic structure of $Rb_3Ni_2(NO_3)_7$ was calculated with the TB-LMTO-ASA (tight-binding linearized muffin-tin orbitals atomic sphere approximation) code [16] and the Vienna *ab initio* simulation package (VASP) [17]. The radii of atomic spheres in the TB-LMTO-ASA calculations were chosen as follows: R(Ni)= 2.3 a.u., R(O)= 1.3–1.6 a.u., R(N)= 1.3–1.4, R(Rb) = 4.4 a.u. A mesh of 32 irreducible k points was used in the VASP calculations. The plane-wave cutoff energy was chosen to be 400 eV. The rotationally invariant form of the local-spin density approximation LSDA+U method with the onsite Coulomb interaction parameter U was utilized [18].

III. RESULTS

A. Crystal structure

Single-crystal x-ray structure determination reveals $Rb_3Ni_2(NO_3)_7$ to crystallize in the orthorhombic space group *Pnma* (No. 62) with the lattice parameters $a = 8.986(1)$, $b = 28.063(3)$, $c = 7.269(1)$ Å, at 200 K. Refinement of 155 parameters gave a goodness-of-fit of 0.970, $R_1 = 0.0315$, and $wR_2 = 0.0616$ on all data. Good agreement of the x-ray diffraction (XRD) pattern of powder, prepared from the sample with the theoretical diffractogram of $Rb_3Ni_2(NO_3)_7$,

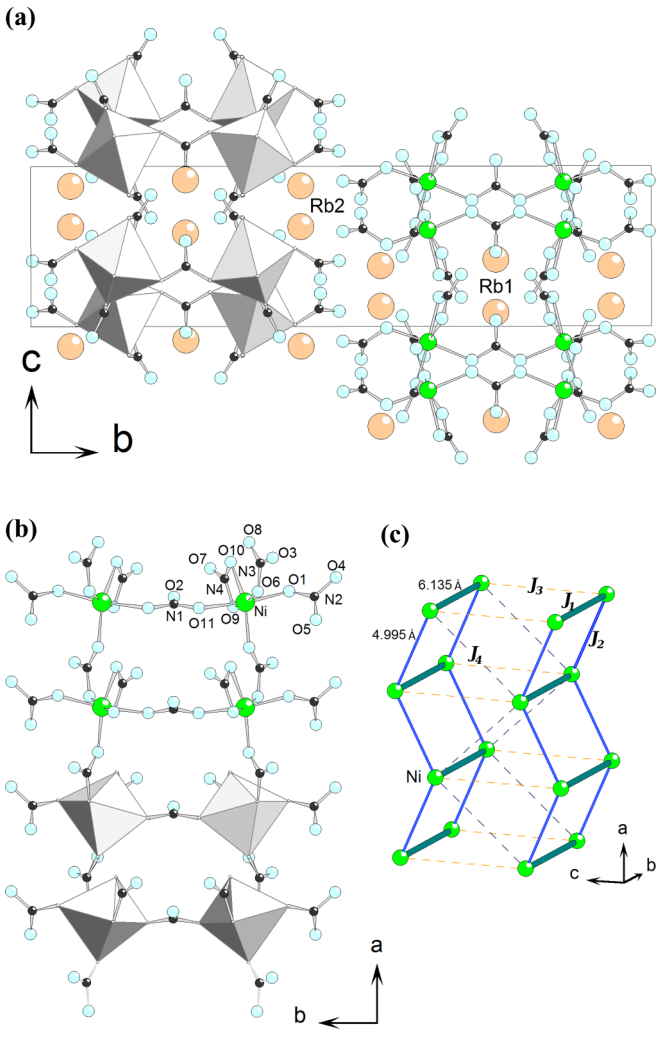

FIG. 1. (a) Projection of the $Rb_3Ni_2(NO_3)_7$ crystal structure along the a direction. (b) The NiO_6 octahedra are connected via NO_3 groups forming zigzag chains along a. Ni, O, N, and Rb atoms are shown as green, cyan, black, and orange spheres, respectively. (c) J_1 and J_2 exchange interactions along the rungs and the legs of the ladders, J_3 and J_4 indicate exchange interactions between the ladders.

calculated according to the crystal structure data, indicates that $Rb_3Ni_2(NO_3)_7$ is the only Ni-containing phase in the obtained sample. The crystal structure parameters and information on the data collection and the structure refinement are given in Table SI in the Supplemental Material [19].

The rubidium-nickel nitrate is isostructural to the previously synthesized $(NH_4)_3Ni_2(NO_3)_7$ compound [13]. The crystal structure of $Rb_3Ni_2(NO_3)_7$ consists of zigzag $[Ni_2(NO_3)_7]_n^{3n-}$ ribbons with Rb^+ ions occupying voids between them. These ribbons have a ladderlike topology, as shown in Fig. 1. The Ni^{2+} ions are surrounded by distorted octahedral polyhedra formed by six oxygen atoms belonging to two terminal (monodentate and bidentate) and three bridging nitrate groups. The $N(1)O_3$ group is located on a mirror plane and connects two nickel atoms by the anti-anti-type forming a rung of the ladder. Along the legs of the ladder, Ni atoms are bonded by means of syn-anti-type $N(3)O_3$ bridges resulting in a Ni . . . Ni distance of 4.995 Å, which is much shorter than the Ni . . . Ni distance of 6.135 Å along the rungs. Selected interatomic distances and bond angles in the crystal structure of $Rb_3Ni_2(NO_3)_7$ are given in Tables SII and SIII in the Supplemental Material [19].

The distances between nickel and nearest oxygen atoms within the NiO_6 octahedra vary from 2.04 to 2.15 Å. In the case of the transition-metal oxides, the magnetic couplings are quite sensitive to the angle of the metal-oxygen-metal bond. In $Rb_3Ni_2(NO_3)_7$, the NiO_6 octahedra are linked through NO_3 groups. The Ni-N-Ni angles along the a and the b axes are 119° and 172°, respectively. It is illustrative to compare these values to NiO (Fm-3m structure). In NiO, the Ni-O distance is 2.1 Å and the Ni-O-Ni angle is 180° which results in a strong antiferromagnetic superexchange interaction of 221 K (19 meV) [20]. Taking into account the strong distortion of the NiO_6 octahedra in $Rb_3Ni_2(NO_3)_7$ and the longer distances between neighboring octahedra coupled by nitrate groups, one could expect that the magnetic exchange interaction in this system should be much weaker than in NiO.

B. Magnetization

The temperature dependence of the magnetic susceptibility $\chi = M/B$ of $Rb_3Ni_2(NO_3)_7$, $B = 0.1$ T, is presented in Fig. 2. In the whole temperature range under study, there is no difference of the measurements obtained in the field-cooled and the zero-field-cooled regime, which evidences the absence of any considerable ferromagnetic impurities. The low-temperature behavior implies only a few quasifree defect spins. The kink in $\chi(T)$ curves at low temperatures appears after short exposure of the sample to air, signaling its deterioration and, possibly, formation of the long-range magnetic order in the regions affected by air moisture. The analysis of the field dependence of the magnetization at small B (not shown) indeed confirms a very small number of quasifree defect spins $S = 1$ of about 0.1%. In the temperature range 50–300 K, the $\chi(T)$ dependence shown in Fig. 2 can be described by a Curie-Weiss–type behavior, $\chi(T) = \chi_0 + C/(T\text{-}\Theta)$, with a temperature-independent term $\chi_0 = 6.6 \times 10^{-4}$ emu/mol, the Curie constant $C = 2.02$ K emu/mol, and the Weiss temperature $\Theta = -10.9$ K. At lower temperatures, $\chi(T)$ deviates from the Curie-Weiss behavior, passes through a maximum at $T_{max} = 11$ K, and subsequently drops more than twice at

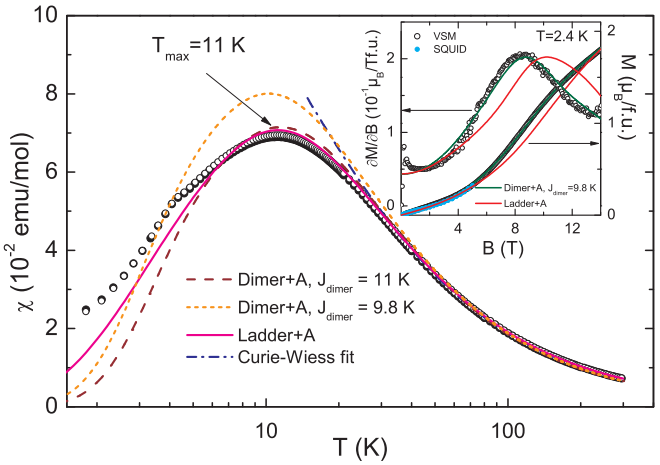

FIG. 2. Temperature dependence of the magnetic susceptibility of $Rb_3Ni_2(NO_3)_7$, at $B = 0.1$ T, taken in the field-cooled regime. A fit in accordance with the Curie-Weiss law (blue dashed-dotted line). The simulation of susceptibility within dimer+A (brown and orange dotted lines) and ladder+A (pink solid line) models (for details, see Sec. III E 3). In the inset: field dependence of the magnetization, at $T = 2.4$ K, and its derivative. The fit within dimer+A model (green line) and a result of the ladder+A model simulation (red line).

$T < T_{max}$. From the Curie constant, the effective magnetic moment $\mu_{eff} = 4.0(2)\ \mu_B$/f.u. is extracted, which for $S = 1$ is associated with the g factor $g = 2.01(5)$. The negative value of the Weiss temperature indicates the predominance of antiferromagnetic exchange interactions at elevated temperatures.

The main magnetic substructures of $Rb_3Ni_2(NO_3)_7$ are the two-leg ladders based on Ni^{2+} ions [cf. Fig. 1(c)]. Depending on the ratio of exchange interaction parameters on the rungs and the legs, this structure's extremities are isolated dimers [21] or uniform chains [22]. The maximum present in $\chi(T)$ can be inherent to each of these cases. Indeed, the experimental data are roughly described in terms of either of these extremal cases by means of analytical expressions for dimers and uniform chains. Fitting the data by means of both models yields the main exchange interaction parameters $J_{dim} = 11$ K (pure dimer model) or $J_{chain} = 8.4$ K (pure chain model). As will be shown in Sec. III E, the generalized ladder model yields a significantly better description of the data.

The magnetization curve $M(B)$ taken in quasistatic magnetic field and its derivative $\partial M(B)/\partial B$ are shown in the inset of Fig. 2. The $M(B)$ curve bends at about $B_C = 10$ T seen as a maximum in the $\partial M/\partial B$ dependence. At $B > B_C$, the magnetization approaches $\sim 2\mu_B$ which is about half of the expected saturation magnetization $M_{sat} \approx 4\mu_B$/f.u. In a dimerlike model, left bending of the magnetization signals field-induced changes of the lowest spin energy state(s) providing information on the energy difference of the singlet and the lowest triplet state. We note that a spin gap in isolated $S = 1$ chains as well as in $S = 1$ spin ladders implies a corresponding anomaly in M vs B, too, as, e.g., seen in $Ni(C_2H_8N_2)_2NO_2ClO_4$ (NENP) model [23]. Quantitatively, the $S = 1$ uniform chain model presumes the magnetic field necessary to overcome energy gap Δ ($\Delta_{chain} = 0.41 J_{chain}$) to be equal to $B = 2.56$ T which is significantly smaller than the experimentally found value.

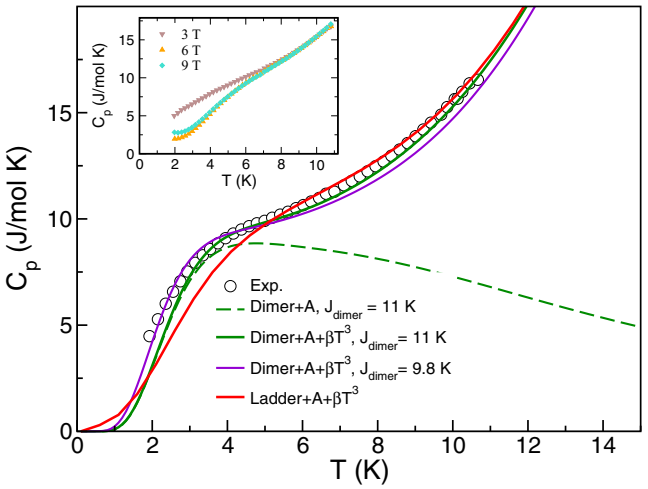

FIG. 3. The temperature dependence of the specific heat of $Rb_3Ni_2(NO_3)_7$ measured at zero magnetic field. The dotted green line was calculated in the model of $S = 1$ dimer+A with $J_{\rm dimer} = 11$ K. Solid green, violet, and red lines represent the sum of the dimer+A with $J_{\rm dimer} = 11$ K, dimer+A with $J_{\rm dimer} = 9.8$ K and ladder+A simulation of the specific heat and a T^3 term, respectively. The inset shows the temperature dependencies of the specific heat in various magnetic fields.

C. Specific heat

The temperature dependencies of the specific heat $C_p(T)$ of $Rb_3Ni_2(NO_3)_7$ taken at various magnetic fields up to 9 T are shown in Fig. 3. The $C_p(T)$ curve at $B = 0$ T clearly shows a low-temperature Schottky anomaly. This anomaly can be attributed to the presence of energetically separated $S = 0$, 1, 2 levels in the energy spectrum of Ni^{2+} dimers which become thermally populated upon heating (cf. Fig. 6). Upon application of external magnetic fields, the ground-state energies are shifted by the Zeeman effect which yields, e.g., the above-mentioned changes of the ground states showing up in the anomaly in $M(B)$. Indeed, the Schottky anomaly clearly changes upon application of external magnetic fields. This effect is most clear if the magnetic field dependence of $C_{\rm p}$ at constant temperature is considered (see Fig. 4). Here, the specific heat is strongly suppressed at about $B = B_{\rm C}$, i.e., it signals the crossing of the ground-state spin levels.

The specific heat calculated for dimer model with anisotropy is shown by the green dotted line in Fig. 3. The lattice contribution to the specific heat was considered by $C_{\rm p}^{\rm lattice} = \beta T^3$, with $\beta = 1943.7\, s/\Theta_{\rm D}^3$. Here, $\Theta_{\rm D}$ is the Debye temperature and $s = 33$ the number of atoms per $Rb_3Ni_2(NO_3)_7$ formula unit. The specific heat of $Rb_3Ni_2(NO_3)_7$ was measured up to 200 K (data not shown) where we obtained $C_{\rm p} \approx 610$ J/(mol K) which is about 75% of the expected Dulong-Petit limit $3Rs = 823$ J/(mol K). Thus, our experimental data imply a lower limit of $\Theta_D > 200$ K for the Debye temperature and accordingly an upper limit for β which is smaller than 0.008 J/(mol K^4). The resulting dimer plus lattice contributions to the specific heat shown by the solid green line in Fig. 3 describe the experimental data quite well in the temperature regime $T > T_{\rm max}$.

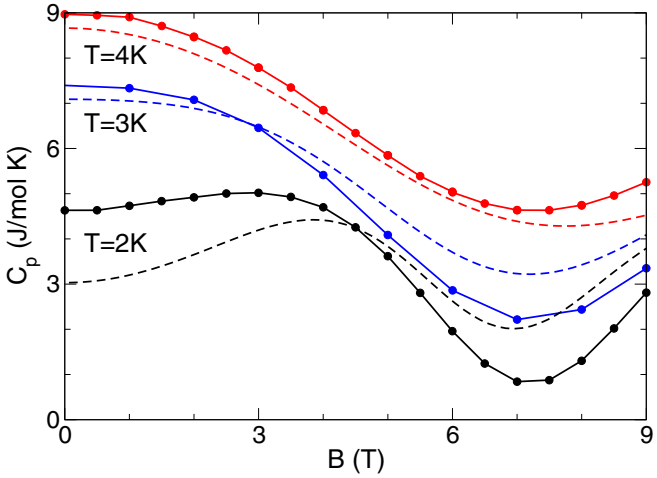

FIG. 4. The field dependencies of the specific heat of $Rb_3Ni_2(NO_3)_7$ at several constant temperatures. The circles are the experimental data, dotted lines show the expected behavior in the dimer+A model.

D. High-frequency ESR spectroscopy

Typical ESR spectra of $Rb_3Ni_2(NO_3)_7$ at $T = 3$ K exhibit broad and separated ESR lines as shown by some examples in Fig. 5 [24]. The spectra allow collecting the respective frequency vs resonance field B_{res} dependencies of the observed lines which are denoted by the red dots. Even without further analysis, the data imply a significant zero-field splitting (ZFS) of around $\Delta \approx 180$ GHz. Although the spectra reflect excitations of a quantum many-body system, similarly to other $S = 1$ quantum spin chains and ladders (see, e.g., [25,26]) the ESR data are well described in terms of the independent dimer+A model of Ni^{2+} spins $S_1 = S_2 = 1$ with uniaxial anisotropy $A_1 = A_2 = A$:

$$\hat{H} = J\hat{\mathbf{S}}_1\hat{\mathbf{S}}_2 + A\left(\hat{S}_1^{z\,2} + \hat{S}_2^{z\,2}\right) + g\mu_B\mathbf{B}(\hat{\mathbf{S}}_1 + \hat{\mathbf{S}}_2). \quad (1)$$

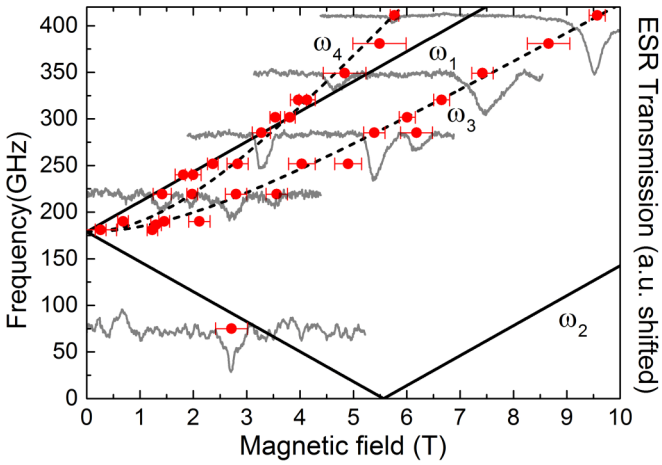

FIG. 5. HF-ESR transmission spectra (shown in gray), at $T = 3$ K, with corresponding resonance positions marked by red dots in the frequency vs magnetic resonance field diagram. The lines are the simulated resonance branches obtained by solving the spin Hamiltonian [Eq. (1)]. Solid lines correspond to $\alpha = 0^\circ$ and dashed ones to $\alpha = 90^\circ$ (see the text).

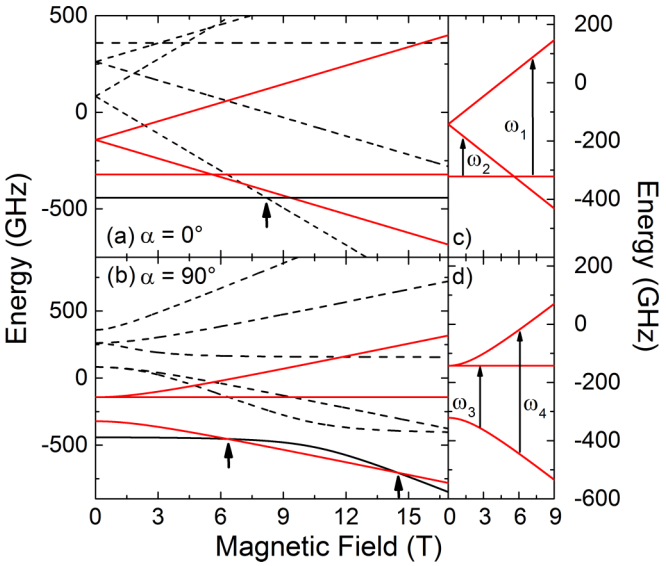

FIG. 6. Energy-level diagrams obtained by solving Eq. (1) for the single-ion anisotropy axis being parallel (a) and orthogonal (b) to the external magnetic field. Black, red, and dashed lines show the singlet, triplet, and quintuplet states, black arrows indicate ground-state level crossing. (c), (d) Show the energy levels of the triplet states in which the observed HF-ESR transitions associated with the resonance branches ω_1 to ω_4 (cf. Fig. 5) occur.

Here, J is the intradimer exchange coupling, B the external magnetic field, and g the effective g factor. Numerical evaluation of the Hamiltonian (1) has been performed by means of the EASYSPINtoolbox for MATLAB [27].

The measured powder sample implies that for a given magnetic field direction, the angle α between B and the local single-ion anisotropy axis varies as $0^\circ \leqslant \alpha \leqslant 90^\circ$. The effect of α on the energy-level diagram is illustrated in Fig. 6 which displays the situation in the extreme cases of the single-ion anisotropy being parallel and orthogonal to the external magnetic field, respectively. Note that without mixing of the spin states, the selection rules $\Delta m_S = \pm 1$ allow transitions only within a given multiplet, while $\Delta S = \pm 1$ (e.g., singlet to triplet transitions) are forbidden. At the temperature of the experiments, transitions within the $S = 2$ quintet states are not observed since the intradimer exchange coupling J results in a too large energy difference between the spin multiplets as compared to the thermal energy, i.e., $E_{\text{triplet}} - E_{\text{quintet}} \ll k_B T$. Thus, in our experiments, allowed transitions are supposed within the triplet states only [see Figs. 6(c) and 6(d)].

The lines in Fig. 5 display the results of the simulations. The solid lines refer to the case $\alpha = 0^\circ$ and the dashed lines to $\alpha = 90^\circ$. The results show that the overall behavior is well described in terms of the dimer model (1). The obtained parameters are the single-ion anisotropy $|A| = 179(1)$ GHz (i.e., 8.6 K) and the isotropic effective g factor of $g = 2.31(5)$, at $T = 3$ K. Although our data do not unambiguously allow determining the sign of A, the following simulations apply a uniaxial case typically observed in distorted octahedrally coordinated Ni^{2+} complexes, i.e., $A < 0$ [26,28–33]. This assumption is corroborated by the temperature dependence of the ω_1-resonance branch (see Fig. S1 in the Supplemental Material [19]) and by the magnetization data (inset of Fig. 2). The size of the anisotropy corresponds well with the recently reported value of -9 K for $Li_2NiW_2O_8$ which is supposed to exhibit spin-1 Ni^{2+} chains [34]. A similar value of the single-ion anisotropy $A = -11.5$ K was also reported for $Na_2Ni_2(C_2O_4)_3(H_2O)_2$ which realizes the spin-1 strong-rung two-leg ladder structure, too [26].

In the frame of the dimer+A model, the calculated energy levels shown in Fig. 6 allow to assign the different branches to particular transitions. At $B = 0$, all observed resonance branches within the $S = 1$ multiplet are degenerated. The resonance branch ω_1 is associated with the transition $m_S = 0 \rightarrow m_S = 1$, and ω_2 with $m_S = -1 \rightarrow m_S = 0$. For $\alpha = 90^\circ$, ω_3 is associated with $m_S = -1 \rightarrow m_S = 0$. Note that the transition $m_S = 0 \rightarrow m_S = 1$ ($\alpha = 90^\circ$) is not observed in the experiment since the $m_S = 0$ spin energy state is considerably above the $m_S = -1$ state and not populated at low temperature [see Fig. 6(d)]. In contrast, the spectra show the presence of the $\Delta m_S = \pm 2$ transition $m_S = -1 \rightarrow m_S = +1$ showing up in the branch ω_4. Accordingly, at high magnetic field the branch ω_4 has almost the double slope as compared to the dipole allowed branches $\omega_1 - \omega_3$ (cf. Ref. [26]). The observed finite intensity of the so-called forbidden transition implies mixing of the pure spin states $m_s = -1, m_s = 0$, and $m_s = +1$ due to crystal-field and spin-orbit effects. The fact that the forbidden transition is clearly observed in the experiment and well described by the independent dimer model somehow supports utilizing a dimer model as for large interdimer coupling, the forbidden transition with $g = 4$ is suppressed. In general, in the case of weak leg coupling, HF-ESR spectra are typically described well in terms of the independent dimer approximation [26,35]. In contrast to the transitions between the triplet states, resonances within higher-spin multiplets are not observed by our HF-ESR measurements, which agrees to large intradimer coupling yielding the higher multiplets energetically well separated from the triplet states.

In general, the solutions of the full many-body quantum spin problem have to be considered when discussing the EPR spectra. It has, however, been shown that in the case of the $S = 1$ 1D Heisenberg antiferromagnet exact diagonalization and perturbation theory qualitatively provide the same results as the dimer model [36,37]. In contrast to the dimer model where the spin chain excitations from the singlet ground state to the triplet excited states are forbidden by EPR selection rules, such resonances are observed, e.g., in NENP. This observation implies considerable mixing which in NENP is associated to the presence of two inequivalent Ni^{2+} sites [25]. As a consequence, the ZFS observed in NENP is determined by single-ion anisotropy D and E as well as by the intrachain coupling J. *A priori* mixing of the states is not excluded in $Rb_3Ni_2(NO_3)_7$. However, the fact that only one gap appears for all observed resonance branches including the forbidden $g = 4$ resonance somehow indicates that the transitions are predominantly dimerlike. In the case of some state mixing, the observed ZFS may be affected by magnetic exchange, too. For weak leg coupling, such contribution would be however small. For the $S = 1$ ladder system with weak leg coupling $Na_2Ni_2(C_2O_4)_2(H_2O)_2$, the validity of the independent dimer model has been proven by quantum Monte Carlo calculations [26]. These simulations performed for several ratios of leg to

rung magnetic exchange show that the magnetic anisotropy determines the ZFS which supports the scenario of predominantly anisotropy governed ZFS in $Rb_3Ni_2(NO_3)_7$.

The field dependence of the spin energy states shown in Fig. 6 is in correspondence with magnetization curve shown in the inset of Fig. 2. For the two extreme angles shown in Fig. 6, the arrows indicate changes of the magnetic ground state. To be specific, at $\alpha = 0^\circ$, there is a field-induced crossing from the $|S = 0, m_S = 0\rangle$ to the $|S = 2, m_S = -2\rangle$ state while at $\alpha = 90^\circ$, the ground state successively changes to different mixed states which evolving from the $|S = 1, m_S = -1\rangle$ and $|S = 2, m_S = -2\rangle$ ones, respectively.

While the dimer+A model of Eq. (1) describes the positions and field dependencies of the resonances sufficiently well, there are deviations with respect to the experimentally observed spectral intensities including splitting of the resonance branches at small and intermediate magnetic fields $B \lesssim 6$ T. These discrepancies imply that a more complex scenario has to be considered to fully describe the magnetic properties of $Rb_3Ni_2(NO_3)_7$, e.g., by including interdimer coupling and transversal anisotropy as well as Dzyaloshinskii-Moriya interactions (see below).

E. Microscopic magnetic model

1. Electronic structure

The partial densities of states (DOS) and band structure obtained in local density approximation (LDA) are shown in Fig. 7. The DOS around the Fermi level is formed by Ni-d states hybridized strongly with O-2p states. The t_{2g}-e_g splitting can be estimated as 1.5 eV, which agrees with that calculated for other nickel oxides (1.1 eV for NiO, 1.7 eV for $Ni(NO_3)_2$ [38]). The splitting of the e_g DOS near the Fermi level is caused by the dimerization accompanied by the formation of the bonding and antibonding states (see Fig. 7). The width of the highest e_g band is about 0.22 eV, hence, the dimer hopping can be estimated as about 110 meV.

To perform a quantitative analysis of the LDA results, we constructed the low-energy model describing the e_g bands near the Fermi level by using the projection procedure [39].

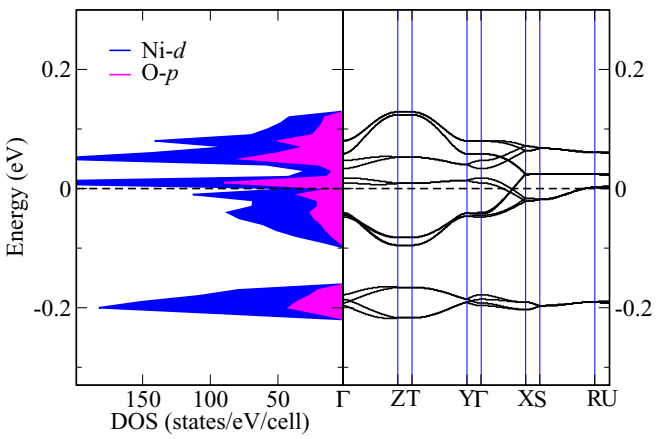

FIG. 7. LDA band structure (e_g bands) around the Fermi level and corresponding partial Ni-d, O-p DOS for $Rb_3Ni_2(NO_3)_7$. The Fermi energy corresponds to $E = 0$.

The average transfer integrals were evaluated as $\bar{t}_m \equiv \bar{t}_{ij} = \sqrt{\mathrm{Tr}(\hat{t}_{ij}\hat{t}_{ij}^T)}$, where $\hat{t}_{ij}$ is the 2×2 matrix in the basis of Wannier functions constructed for the e_g bands and the trace is taken over orbital indices. The notation of the hopping integrals $\bar{t}_m$ (m = 1–4) corresponds to the notation of the main exchange paths shown in Fig. 1(c). We obtain $\bar{t}_1 = 110$ meV, $\bar{t}_2 = 47$ meV, $\bar{t}_3 = 3$ meV, $\bar{t}_4 = 15$ meV. From these results one can already assume that $Rb_3Ni_2(NO_3)_7$ can be classified as a spin-1 two-leg ladder compound.

The metallic ground state of $Rb_3Ni_2(NO_3)_7$ obtained within LDA (see Fig. 7) is a standard problem of this approach which is due to the underestimation of the onsite Coulomb correlations. To resolve it, we implement the LDA+U method [40]. The values of the onsite Coulomb repulsion parameter and the intra-atomic Hund's rule exchange interaction were chosen to be $U = 6.5$–7 eV and $J_H = 0.95$ eV. As will be shown below, such a parameter choice leads to a good agreement between experiment and theory on the magnetic susceptibility. Moreover, these parameters are close to those estimated within the LDA constrained procedure for other nickel oxides [41,42]. Since the Curie-Weiss temperature of $Rb_3Ni_2(NO_3)_7$ is negative, antiferromagnetic arrangement of magnetic moments on Ni ions was imposed in the LDA+U calculation. We obtained an insulating ground state (LDA+U DOS is shown in Fig. S2 in the Supplemental Material [19]) with the magnetic moment of 1.87–1.91μ_B per Ni and an energy gap of 2.06–2.11 eV for $U = 6.5$–7 eV. The value of the magnetic moment is in correspondence with typical values for nickel oxides (1.9μ_B for NiO [43]). The value of the energy gap conforms to a green color of the crystals of $Rb_3Ni_2(NO_3)_7$.

2. Magnetic interactions

To describe the magnetic properties of the $Rb_3Ni_2(NO_3)_7$ system on the level of the first-principles calculations, we mainly concentrate on the isotropic exchange interaction within the spin Hamiltonian

$$H = \sum_{ij} J_{ij} \hat{\mathbf{S}}_i \hat{\mathbf{S}}_j, \tag{2}$$

where J_{ij} is the isotropic exchange interaction.

Parameters of the spin Hamiltonian were calculated by using the magnetic force theorem. For the isotropic exchange interactions, we used the approach reported in Refs. [44,45], which is based on the infinitesimal rotation of the magnetic moments from the antiferromagnetic ground state. A similar procedure based on the mixed type of the perturbation theory on the spin-orbit coupling and infinitesimal rotation of the magnetic moments [46] can be used to calculate the Dzyaloshinskii-Moriya interaction favoring the orthogonal magnetic orientation of the spins. However, as we will show below, such couplings are very weak in comparison with the isotropic exchange interaction and can be excluded from the further consideration.

The main isotropic exchange pathways for $Rb_3Ni_2(NO_3)_7$ are shown in Fig. 1(c), where J_1 and J_2 are the couplings along the rungs and the legs of the ladder, respectively. J_3 and J_4 denote the exchange interactions between the ladders. The calculated values of the exchange integrals are $J_1 = 11$–9.84 K, $J_2 = 1.62$–1.44 K, $J_3 = 0$ K, and $J_4 = 0.07$ K for the

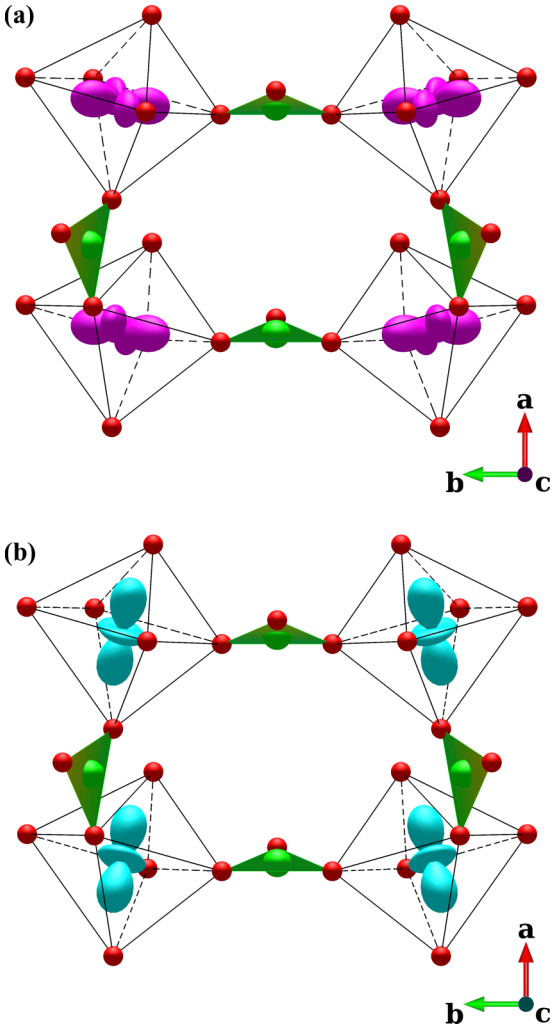

FIG. 8. The e_g orbitals corresponding to the largest elements in the matrix of exchange integrals for exchange along the rung (a) and leg (b) of the ladder determine J_1 and J_2, respectively.

chosen range of the onsite Coulomb repulsion parameter. All exchange interactions are antiferromagnetic. According to the calculated exchange constants, we classify $Rb_3Ni_2(NO_3)_7$ as a spin-1 two-leg ladder compound. The obtained ratio $\frac{J_2}{J_1} = 0.15$ indicates very strong rung interaction. This ratio is about two times smaller than what was experimentally found for the spin-$\frac{1}{2}$ ladder analog $(C_5H_{12}N)_2CuBr_4$ [47].

In order to understand the quantitative difference between J_1 and J_2, we are going to analyze the partial orbital contributions from different Ni-d orbitals to the matrix of the exchange integrals. The largest elements in this matrix for the J_1 and J_2 pathways correspond to the exchange between the orbitals shown in Figs. 8(a) and 8(b), respectively. From Fig. 8(a), it is clearly seen that these orbitals have $(x^2 - y^2)$-like symmetry and their lobes are pointing towards the oxygen atoms along b axis forming σ bonds. The p orbitals of the oxygen ions are strongly overlapping with these orbitals which leads to a strong antiferromagnetic interaction J_1.

The orbitals which determine the J_2 exchange along the legs of the ladder have $(3z^2 - r^2)$-like symmetry [Fig. 8(b)]. J_2 is much smaller than J_1 since the lobes of the $(3z^2 - r^2)$-like orbitals on the two Ni^{2+} ions along the legs (i.e., in a direction) tilt in different directions. The p orbital pointing towards the $3z^2 - r^2$ orbital on one particular Ni^{2+} ion will be directed almost perpendicular to the $3z^2 - r^2$ orbital of the neighboring Ni^{2+} ion in the leg. Such geometry results in a rather weak $3z^2 - r^2$ O-p overlap leading to an exchange constant seven times smaller than J_1. In comparison, the interladder interactions J_3 and J_4 are negligible since there are no nitrate groups between Ni atoms in these directions and the Ni-Ni distances are large, i.e., 7.3 and 6.8 Å, respectively.

These TB-LMTO-ASA results concerning the isotropic exchange interactions are confirmed by the GGA+U VASP calculations. We have evaluated the exchange integral along the rungs (J_1) by the total energy difference of ferromagnetic and antiferromagnetic configurations $J_1 = \frac{E_{FM} - E_{AFM}}{8S^2}$. The antiferromagnetic configuration has the lower total energy and the magnetic moment on the Ni^{2+} ion is $1.78\mu_B$ in accordance with the results of the LMTO calculations. The obtained energy gap, however, amounts to 3.1 eV and is larger than the one obtained within LMTO. The value of the exchange interaction $J_1 = 12.73$ K agrees with the TB-LMTO-ASA results.

The center of inversion in the *Pnma* structure of $Rb_3Ni_2(NO_3)_7$ is placed at the origin. Since two Ni atoms belonging to the rungs or the legs of the ladder do not transform into each other under inversion operation, one could expect a nonzero Dzyaloshinskii-Moriya (DM) interaction for these two pathways. Indeed, we obtain $\vec{D}_1 = (0.01,0,0.01)$ K and $\vec{D}_2 = (-0.01,0.1,0.08)$ K. Note, however, that our experimental data on the powder sample do not allow evidencing such a small effect of the DM exchange.

Although a single-ion anisotropy of the same order of magnitude as the rung-exchange coupling was derived from the ESR spectra analysis, we restrict ourselves to the calculation of the isotropic exchange interactions. In $Rb_3Ni_2(NO_3)_7$, NiO_6 octahedra are strongly distorted and the easy axis could have either direction. To derive the direction and to calculate the value of single-ion anisotropy, one has to rotate the spin moment on one Ni atom in different directions by fixing all other moments in order to get the energy profile versus angle of rotation. Such calculations are, however, out of the scope of this paper.

3. Comparison with experiment

To compare theoretical results on exchange interaction parameters with experiment, we employ the expression for the Curie-Weiss temperature $\Theta = J_0 S(S+1)/3k_B$ obtained by using the high-temperature expansion of the magnetic susceptibility. Here, J_0 is the summarized exchange interaction of a given Ni site with the magnetic environment, which is $J_0 = J_1 + 2J_2 + 2J_3 + 2J_4$ in case of $Rb_3Ni_2(NO_3)_7$. The value of the Curie-Weiss temperature recalculated from the numerically obtained exchange constants equals -9.0 K (for $U = 6.8$ eV) which is in a good agreement with the experimental data of $\Theta = -10.9$ K.

According to the calculated exchange interaction parameters and strong uniaxial anisotropy revealed by HF-ESR study, the full spin model for the $Rb_3Ni_2(NO_3)_7$ system should be the ladder model with uniaxial anisotropy. Verification

of this model is impeded since all measurements were done on powder samples, i.e., for comparison with experiment one has to average over the angle α between magnetic field direction and the local single-ion anisotropy axis. Introducing such an averaging for the full model is not trivial within the ALPS simulation package [48,49], hence, in the analysis of experimental data we used two models. One is the independent dimer model with anisotropy which could be solved exactly (denoted as dimer+A model). In order to imitate the powder sample, we apply the average over the angle α. The second one is the ladder model with anisotropy (denoted as ladder+A model). For this model, the simple averaging in the form of weighted sum of $\frac{1}{3}$ longitudinal and $\frac{2}{3}$ transverse components was used. Here, the longitudinal component corresponds to the solution of the model in magnetic field directed along Z axis, while the transverse one corresponds to magnetic field along X or Y, the anisotropy axis is along Z in both cases.

The results of magnetic susceptibility simulation obtained within dimer+A model with $J_{\text{dimer}} = 11$ K (brown dotted line), $J_{\text{dimer}} = 9.8$ K (orange dotted line), and ladder+A model with $J_1 = 10.16$ K, $J_2 = 1.5$ K (pink solid line) are shown in Fig. 2. One can see that the ladder+A model provides better agreement with experimental data. In Fig. S3 in the Supplemental Material [19] we also demonstrate the effect of anisotropy on the susceptibility in the dimer+A model. The susceptibilities of the dimer+A model with A along X and Z axis are quite different (blue and orange curves), but the longitudinal and transverse parts almost compensate each other when being averaged (red curve). Hence, the susceptibility of the powder-averaged dimer+A model (dotted violet curve) looks almost identical to the one of the Heisenberg dimer without any anisotropy (green curve).

It is worth mentioning that the leg exchange $J_2 = 1.5$ K is rather small. Any small coupling between dimers would give the very same susceptibility (such a small correction can be treated perturbatively within the random phase approximation (RPA) approach). This is why the first-principle calculations are in the end crucial for pinpointing the direction of the inter-dimer coupling and identifying the model as the ladder one.

The simulations of magnetization and its derivative for the dimer+A and ladder+A models are shown in the inset of Fig. 2 by green and red lines, respectively. By using the values of A and g from the analysis of the HF-ESR data, the magnetization data were fitted yielding $J_{\text{dimer}} = 9.7(8)$ K. The simulation within ladder+A model with $J_1 = 10.16$ K, $J_2 = 1.5$ K provides rather moderate correspondence with experimental data. At this point, we would like to mention that the magnetization simulated with fine averaging over α differs substantially from the sum of the $\frac{1}{3}$ longitudinal and $\frac{2}{3}$ transverse components. In order to illustrate this point, the comparison of the different types of averaging for dimer+A model is presented in Fig. S4 in the Supplemental Material [19].

The results of simulations of specific heat summed with T^3 term for dimer+A with $J_{\text{dimer}} = 11$ K, $J_{\text{dimer}} = 9.8$ K and ladder+A with $J_1 = 10.16$ K, $J_2 = 1.5$ K are shown in Fig. 3 as green, violet, and red lines, respectively. The $S = 1$ dimer+A model with $J_{\text{dimer}} = 11$ K results in better agreement with the experimental $C_p(T)$ data.

The dimer+A model seems to be the minimal model for understanding thermodynamic properties of $Rb_3Ni_2(NO_3)_7$, though we were not able to reproduce all experimental data within this model using the same exchange parameter J_{dimer}. Simulation of susceptibility, magnetization, and specific heat within the ladder+A model with the same set of exchange interactions $J_1 = 10.16$ K, $J_2 = 1.5$ K provides decent description of the experimental results. The most apparent source of the deviation from experiment is an oversimplified form of averaging implemented for imitation of powder samples in the case of ladder+A model.

IV. DISCUSSION

In contrast to the variety of weakly coupled Haldane chain systems, there are only few examples of $S = 1$ ladder systems with predominant rung coupling which have been studied by HF-ESR, namely, $Na_2Ni_2(C_2O_4)_2(H_2O)_2$ and $Na_2Fe_2(C_2O_4)_2(H_2O)_2$, the latter being described by a fictitious spin $S = 1$ with strongly anisotropic g factor [26,35]. In both cases, the data have been appropriately described in terms of the independent dimer model. These two materials show $J = 43$ and 20 K, respectively, while $A = 11.5$ K (planar) and -22 K (axial). Interestingly, although negative uniaxial anisotropy in the Ni^{2+} systems is discussed as a potential route to bistable molecular magnets, there are only few examples in the literature where $A < 0$ has been experimentally shown [50–52].

The anisotropy parameter obtained by describing the HF-ESR data by means of the dimer+A model agrees to what has been found in other low-dimensional Ni^{2+} compounds. In this class of systems, the most studied by means of HF-ESR are $S = 1$ Heisenberg antiferromagnetic chains, viz., Haldane chains, such as NENP [25] or DTN [53]. In contrast to the weakly coupled dimer scenario realized in $Rb_3Ni_2(NO_3)_7$, these materials exhibit intrachain couplings much larger than the interchain ones. Depending on the actual bonding geometries and distances, a large variety of intrachain couplings are found, i.e., ranging from sub-Kelvin and Kelvin in NENC, NBYC, or DTN [53,54] to about 45 K in the typical Haldane systems NENP, NINO, and NENB [55,56].

The anisotropy obtained from magnetization and ESR measurements is typically a few K in these materials, as seen in NBYC (2.6 K), DTN (8.9 K), and NENP (7.3 K) [53–55]. In all these examples, however, anisotropy is plane type in contrast to what is seen in $Rb_3Ni_2(NO_3)_7$. In addition, the HF-ESR data of these materials usually show several zero-field gaps, i.e., splitting of the ω_2 and ω_4 modes at $B = 0$ T. This implies the presence of significant E anisotropy which can be neglected in the description of the HF-ESR data presented here.

V. CONCLUSIONS

In summary, we report the synthesis, crystal structure, and thermodynamic properties of the $Rb_3Ni_2(NO_3)_7$ compound. The magnetic excitations have been examined in high-field high-frequency ESR. While the crystal structure was determined on single crystals, the thermodynamic properties were obtained on powder samples. The crystal structure implies a two-leg ladderlike arrangement of Ni^{2+} ions in $Rb_3Ni_2(NO_3)_7$, i.e., suggesting the scenario of $S = 1$ spin ladders. Our measurements of magnetization, specific heat, and high-field

electron spin resonance indeed reveal a spin-gapped quantum ground state. This ground state in $Rb_3Ni_2(NO_3)_7$ is quite fragile. Even short exposure of the sample to air may lead to formation of long-range order at low temperature. Tentatively, this side effect concerns only a small part of the sample since no magnetic phase transitions were detected in specific-heat measurements.

Our analysis of the experimental magnetic susceptibility data and electronic structure calculations shows that the main exchange interaction along the rung of the ladder amounts to 10.2 K while the interaction along the leg is about seven times smaller. In addition, the HF-ESR and magnetization data imply a strong uniaxial anisotropy $|A| = 8.6$ K. Hence, we can identify $Rb_3Ni_2(NO_3)_7$ as the physical realization of the strong-rung spin-1 ladder model with single-ion anisotropy which may be described in terms of a valence-bond solid. Such detailed information on thermodynamic properties and appropriate spin model could be useful for investigation of quantum phenomena in $Rb_3Ni_2(NO_3)_7$ under external magnetic field.

ACKNOWLEDGMENTS

We thank A. A. Tsirlin for useful discussions. The work of V.V.M. was supported by the Russian Science Foundation through the Project No. 14-12-00306. Financial support by the DFG via Project No. KL1824/13 is gratefully acknowledged. J.W. acknowledges support by the IMPRS-QD and by the HGSFP. A.N.V. and O.S.V. acknowledge support by Russian Foundation for Basic Research Grants No. 16-02-00021 and No. 17-02-00211. This work was supported in part from the Ministry of Education and Science of the Russian Federation in the framework of Increase Competitiveness Program of NUST "MISiS" (Grant No. K2-2017-084) and by Act 211 of the Government of Russian Federation, Agreements No. 02.A03.21.0004, No. 02.A03.21.0006, and No. 02.A03.21.0011. E.B.D. acknowledges the financial support of RFBR Grant No. 6-33-01131-a. Z.V.P. acknowledges the financial support from FASO of Russia (theme "Spin") Grant No. AAAA-A18-118020290104-2 and Project No. UrO RAN 18-10-2-37.

[1] V. V. Mazurenko, M. V. Valentyuk, R. Stern, and A. A. Tsirlin, Phys. Rev. Lett. **112**, 107202 (2014).
[2] H. Kageyama, K. Yoshimura, R. Stern, N. V. Mushnikov, K. Onizuka, M. Kato, K. Kosuge, C. P. Slichter, T. Goto, and Y. Ueda, Phys. Rev. Lett. **82**, 3168 (1999).
[3] H. D. Rosales, D. C. Cabra, and P. Pujol, Phys. Rev. B **92**, 214439 (2015).
[4] E. Dagotto and T. M. Rice, Science **271**, 618 (1996).
[5] D. Allen and D. Sénéchal, Phys. Rev. B **61**, 12134 (2000).
[6] F. B. Ramos and J. C. Xavier, Phys. Rev. B **89**, 094424 (2014).
[7] F. Pollmann, E. Berg, A. M. Turner, and M. Oshikawa, Phys. Rev. B **85**, 075125 (2012).
[8] J. Schliemman and A. M. Läuchli, J. Stat. Mech. (2012) P11021.
[9] K. Wierschem and P. Sengupta, Phys. Rev. Lett. **112**, 247203 (2014).
[10] S. Suh, K. A. Al-Hassanieh, E. C. Samulon, I. R. Fisher, S. E. Brown, and C. D. Batista, Phys. Rev. B **84**, 054413 (2011).
[11] V. S. Zapf, D. Zocco, B. R. Hansen, M. Jaime, N. Harrison, C. D. Batista, M. Kenzelmann, C. Niedermayer, A. Lacerda, and A. Paduan-Filho, Phys. Rev. Lett. **96**, 077204 (2006).
[12] S. Mukhopadhyay, M. Klanjšek, M. S. Grbić, R. Blinder, H. Mayaffre, C. Berthier, M. Horvatić, M. A. Continentino, A. Paduan-Filho, B. Chiari, and O. Piovesana, Phys. Rev. Lett. **109**, 177206 (2012).
[13] I. V. Morozov, A. A. Fedorova, T. A. Rodionova, and S. I. Troyanov, Russ. J. Inorg. Chem. **48**, 985 (2003).
[14] R. Klingeler, B. Büchner, K.-Y. Choi, V. Kataev, U. Ammerahl, A. Revcolevschi, and J. Schnack, Phys. Rev. B **73**, 014426 (2006).
[15] P. Comba, M. Großhauser, R. Klingeler, C. Koo, Y. Lan, D. Müller, J. Park, A. Powell, M. J. Riley, and H. Wadepohl, Inorg. Chem. **54**, 11247 (2015).
[16] O. K. Andersen and O. Jepsen, Phys. Rev. Lett. **53**, 2571 (1984).
[17] G. Kresse and J. Furthmüller, Phys. Rev. B **54**, 11169 (1996).
[18] A. I. Liechtenstein, V. I. Anisimov, and J. Zaanen, Phys. Rev. B **52**, R5467(R) (1995).
[19] See Supplemental Material at http://link.aps.org/supplemental/10.1103/PhysRevB.97.144420 for the details of crystallographic data, LDA+U densities of states, simulation of susceptibility, and magnetization within dimer+A model.
[20] M. T. Hutchings and E. J. Samuelsen, Phys. Rev. B **6**, 3447 (1972).
[21] R. L. Carlin, *Magnetochemistry* (Springer, Berlin, 1986).
[22] J. M. Law, H. Benner, and R. K. Kremer, J. Phys.: Condens. Matter **25**, 065601 (2013).
[23] T. Takeuchi, M. Ono, H. Hori, T. Yosida, A. Yamagishi, and M. Date, J. Phys. Soc. Jpn. **61**, 3255 (1992).
[24] At higher fields between 10 and 16 T, no further resonances were detected at the measurement frequencies.
[25] W. Lu, J. Tuchendler, M. von Ortenberg, and J. P. Renard, Phys. Rev. Lett. **67**, 3716 (1991).
[26] C. Mennerich, H.-H. Klauss, M. Broekelmann, F. J. Litterst, C. Golze, R. Klingeler, V. Kataev, B. Büchner, S.-N. Grossjohann, W. Brenig *et al.*, Phys. Rev. B **73**, 174415 (2006).
[27] S. Stoll and A. Schweiger, J. Magn. Reson. **178**, 42 (2006).
[28] J. Krzystek, A. Ozarowski, and J. Telser, Coord. Chem. Rev. **250**, 2308 (2006).
[29] Y. Krupskaya, A. Alfonsov, A. Parameswaran, V. Kataev, R. Klingeler, G. Steinfeld, N. Beyer, M. Gressenbuch, B. Kersting, and B. Büchner, ChemPhysChem **11**, 1961 (2010).
[30] A. Das, K. Gieb, Y. Krupskaya, S. Demeshko, S. Dechert, R. Klingeler, V. Kataev, B. Büchner, P. Müller, and F. Meyer, J. Am. Chem. Soc. **133**, 3433 (2011).
[31] E. A. Popova, R. Klingeler, N. Tristan, B. Büchner, and A. N. Vasiliev, Phys. Rev. B **85**, 174402 (2012).
[32] E. A. Popova, S. A. Klimin, M. N. Popova, R. Klingeler, N. Tristan, B. Büchner, and A. N. Vasiliev, J. Magn. Magn. Mater. **331**, 133 (2013).
[33] Y. Yamaguchi, J. Phys. Soc. Jpn. **29**, 1163 (1970).
[34] K. M. Ranjith, R. Nath, M. Majumder, D. Kasinathan, M. Skoulatos, L. Keller, Y. Skourski, M. Baenitz, and A. A. Tsirlin, Phys. Rev. B **94**, 014415 (2016).

[35] H. Yamaguchi, S. Kimura, Z. Honda, K. Okunishi, S. Todo, K. Kindo, and M. Hagiwara, J. Phys. Soc. Jpn. **78**, 124701 (2009).
[36] K. Katsumata and Koichi, J. Phys.: Condens. Matter **12**, R589 (2000).
[37] O. Golinelli, Th. Jolicoeur, and R. Lacaze, J. Phys.: Condens. Matter **5**, 7847 (1993).
[38] O. S. Volkova, V. V. Mazurenko, I. V. Solovyev, E. B. Deeva, I. V. Morozov, J.-Y. Lin, C. K. Wen, J. M. Chen, M. Abdel-Hafiez, and A. N. Vasiliev, Phys. Rev. B **90**, 134407 (2014).
[39] V. I. Anisimov, D. E. Kondakov, A. V. Kozhevnikov, I. A. Nekrasov, Z. V. Pchelkina, J. W. Allen, S.-K. Mo, H.-D. Kim, P. Metcalf, S. Suga *et al.*, Phys. Rev. B **71**, 125119 (2005).
[40] V. Anisimov, F. Aryasetiawan, and A. Lichtenstein, J. Phys.: Condens. Matter **9**, 767 (1997).
[41] V. I. Anisimov, J. Zaanen, and O. K. Andersen, Phys. Rev. B **44**, 943 (1991).
[42] F. Tran, P. Blaha, K. Schwarz, and P. Novák, Phys. Rev. B **74**, 155108 (2006).
[43] A. K. Cheetham and D. A. O. Hope, Phys. Rev. B **27**, 6964 (1983).
[44] A. I. Lichtenstein, M. I. Katsnelson, V. P. Antropov, and V. A. Gubanov, J. Magn. Magn. Mater. **67**, 65 (1987).
[45] V. V. Mazurenko and V. I. Anisimov, Phys. Rev. B **71**, 184434 (2005).
[46] V. V. Mazurenko, Y. O. Kvashnin, Fengping Jin, H. A. De Raedt, A. I. Lichtenstein, and M. I. Katsnelson, Phys. Rev. B **89**, 214422 (2014).
[47] A. V. Sologubenko, T. Lorenz, J. A. Mydosh, B. Thielemann, H. M. Rønnow, Ch. Rüegg, and K. W. Krämer, Phys. Rev. B **80**, 220411 (2009).
[48] B. Bauer, L. D. Carr, H. G. Evertz, A. Feiguin, J. Freire, S. Fuchs, L. Gamper, J. Gukelberger, E. Gull, S. Guertler *et al.*, J. Stat. Mech. (2011) P05001.
[49] A. F. Albuquerque, F. Alet, P. Corboz, P. Dayal, A. Feiguin, S. Fuchs, L. Gamper, E. Gull, S. Gürtler, A. Honecker *et al.*, J. Magn. Magn. Mater. **310**, 1187 (2007).
[50] E. C. Yang, C. Kirman, J. Lawrence, L. N. Zakharov, A. L. Rheingold, S. Hill, and D. N. Hendrickson, Inorg. Chem. **44**, 3827 (2005).
[51] E. C. Yang, W. Wernsdorfer, S. Hill, R. S. Edwards, M. Nakano, S. Maccagnano, L. N. Zakharov, A. L. Rheingold, G. Christou, and D. N. Hendrickson, Polyhedron **22**, 1727 (2003).
[52] Y. Krupskaya, A. Alfonsov, A. Parameswaran, V. Kataev, R. Klingeler, G. Steinfeld, N. Beyer, M. Gressenbuch, B. Kersting, and B. Büchner, ChemPhysChem **11**, 1961 (2010).
[53] S. A. Zvyagin, J. Wosnitza, C. D. Batista, M. Tsukamoto, N. Kawashima, J. Krzystek, V. S. Zapf, M. Jaime, N. F. Oliveira, Jr., and A. Paduan-Filho, Phys. Rev. Lett. **98**, 047205 (2007).
[54] M. T. Batchelor, X. W. Guan, N. Oelkers, and A. Foerster, J. Stat. Mech. (2004) P10017.
[55] M. Sieling, U. Löw, B. Wolf, S. Schmidt, S. Zvyagin, and B. Lüthi, Phys. Rev. B **61**, 88 (2000).
[56] E. Čižmáar, M. Ozerov, O. Ignatchik, T. P. Papageorgiou, J. Wosnitza, S. A. Zvyagin, J. Krzystek, Z. Zhou, C. P. Landee, B. R. Landry *et al.*, New J. Phys. **10**, 033008 (2008).